Michigan State University

National Superconducting Cyclotron Laboratory

AZIMUTHAL CORRELATIONS AS A TEST FOR CENTRALITY IN HEAVY ION COLLISIONS

L. PHAIR, D.R. BOWMAN, N. CARLIN, C.K. GELBKE, W.G. GONG, Y.D. KIM, M.A. LISA, W.G. LYNCH, G.F. PEASLEE, R.T. de SOUZA, M.B. TSANG, C. WILLIAMS, F. ZHU, N. COLONNA, K. HANOLD, M.A. McMAHON, and G.J. WOZNIAK

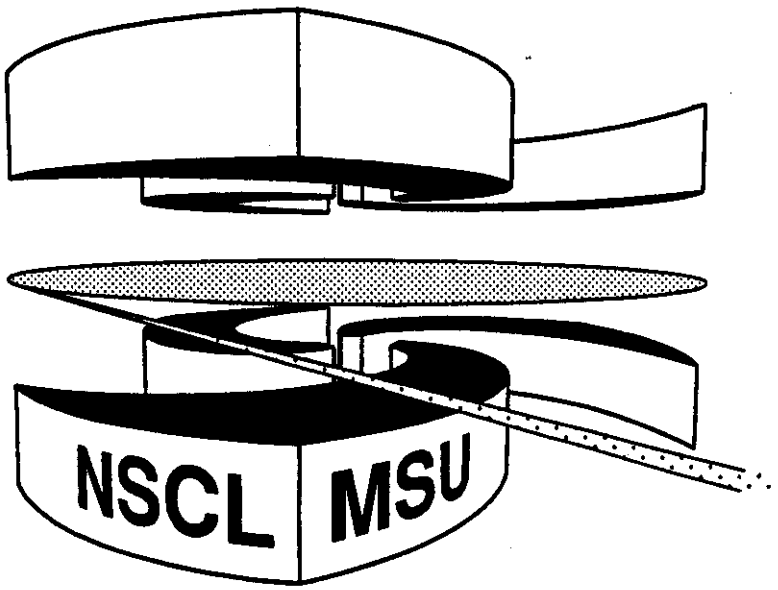

MSUCL-886 **MARCH 1993**

MSUCL-886
March, 1993

Azimuthal Correlations as a Test for Centrality in Heavy Ion Collisions

L. Phair, D.R. Bowman*, N. Carlin[2], C.K. Gelbke, W.G. Gong[3], Y.D. Kim[4], M.A. Lisa, W.G. Lynch, G.F. Peaslee, R.T. de Souza[5], M.B. Tsang, C. Williams and F. Zhu[6]

National Superconducting Cyclotron Laboratory
and Department of Physics and Astronomy
Michigan State University, East Lansing, MI 48824, USA

N. Colonna[7], K. Hanold, M.A. McMahan, and G.J. Wozniak

Nuclear Science Division and Accelerator and Fusion Research Division,
Lawrence Berkeley Laborato y, Berkeley, CA 94720, USA

Abstract:

Azimuthal correlations of particles emitted in collisions between ^{197}Au target nuclei and projectiles ^{36}Ar (at E/A=35, 50, 80 and 110 MeV) and ^{129}Xe (at E/A=50 MeV) have been measured with the MSU Miniball, a 4π phoswich array with a low detection threshold. Various impact parameter filters, based on the charged particle multiplicity, transverse energy and midrapidity charge are tested by their ability to suppress collective motion as measured by the azimuthal correlations. The usefulness of a directivity cut in selecting central collisions for these systems is evaluated.

---

1 Present Address: Chalk River Laboratories, Chalk River, Ontario KOJ 1J0, Canada.
2 Present Address: Instituto de Fisica, Universidade de Sao Paulo, C. Postal 20516, CEP 01498, Sao Paulo, Brazil.
3 Present Address: Lawrence Berkeley Laboratory, University of California, Berkeley, CA 94720.
4 Present Address: National Laboratory for High Energy Physics, l-l Oho, Tsukuba, Ibaraki 305, Japan
5 Present Address: Indiana University Cyclotron Facility and Department of Chemistry, Indiana University, Bloomington, IN 47405
6 Present Address: Brookhaven National Laboratory, Upton, Long Island, NY 11973
7 Present Address: Instituto Nazionale Fisica Nucleare, V. Amendola, Bari, Italy

1. Introduction

Intermediate energy nucleus-nucleus collisions may produce finite nuclear systems at temperatures and densities commensurate with a liquid-gas phase transition in infinite nuclear matter. Calculations indicate that many promising signatures are strongly influenced by the impact parameter [1]. Such dependencies are difficult to unravel in inclusive experiments because of the averaging over impact parameter. Better comparisons between experiment and theory can be made when one focuses on exclusive measurements where reaction filters are used to select narrow ranges of impact parameter. For studies addressing the thermodynamical properties of nuclear matter, the selection of central collisions is of particular interest since reaction zones formed in central collisions promise to reach the largest degree of equilibration.

In most experiments, information about the impact parameter is extracted from quantities which relate to the violence of the collision. e.g. the total charged particle multiplicity N_C [1-4], the total transverse energy E_t [5] of the emitted charged particles, or the multiplicity of emitted hydrogen nuclei N_1 (the complement of Z_{bound} [6], the summed charge of emitted particles with $Z \geq 2$). Some impact parameter filters utilize kinematic cuts to reduce contamination from spectator nuclei. For example one may use the summed charge of particles emitted at midrapidity [7]. In a previous paper we have shown [8] that impact parameter techniques based upon these different observables provide rather similar event selection and that, indeed, cuts on small deduced impact parameters strongly suppress contributions from projectile-like fragments as expected from qualitative arguments. A recent analysis of data with solid angle coverage restricted to forward angles ($\theta_{lab} \leq 30°$) suggests that improved selectivity for central collisions could be achieved by introducing a new

observable, the transverse momentum directivity (defined in Eq. 6, below) and by simultaneous cuts on large charged-particle multiplicities and small transverse-momentum directivities [9].

In this paper, we address two questions: (i) Can previously used impact parameters filters (N_C, E_t, and Z_Y) be used to select central collisions, i.e. collisions with small angular momenta? (ii) Do cuts on the directivity significantly improve central event selection when used with detectors providing 4π coverage? In order to quantify the selection of collisions with small impact parameters, we explore the azimuthal correlations between emitted light particles [10-16]. For truly central collisions, a reaction plane is undefined and the azimuthal distribution of emitted particles must be symmetric about the beam axis. If the azimuthal correlations between two emitted particles reflect their single-particle emission patterns, the azimuthal correlation function must become flat for central collisions. (Deviations from strict azimuthal isotropy may arise from final state interactions such as the sequential decay of primary reaction products produced in particle unbound states [17] or, for small systems, from momentum conservation effects [11,18].) For peripheral collisions on the other hand, transverse flow effects or other ordered motion in the reaction plane [10-16, 19-23] can cause large anisotropies in the azimuthal correlations. We apply this analysis to our previously measured [8,23-27] data of $^{36}Ar+^{197}Au$ collisions at E/A=35, 50, 80 and 110 MeV, and $^{129}Xe+^{197}Au$ collisions at E/A=50 MeV.

The paper is organized as follows. A brief summary of experimental details is given in section 2. In section 3 we define the various impact parameter filters. In section 4 we define the azimuthal correlations that will be used in section 5 to test the effectiveness of the different impact parameter filters. In section 6 we

explore the usefulness of a directivity cut in selecting central collisions. A summary and conclusions are given in section 7.

2. Experimental setup

The experiments were performed with ^{36}Ar and ^{129}Xe beams extracted from the K500 and K1200 cyclotrons at the National Superconducting Cyclotron Laboratory of Michigan State University. The argon beam energies were E/A=35, 50, 80 and 110 MeV, and extracted intensities were typically 10^8 particles per second. The xenon beam energy was E/A=50 MeV with intensities of about 10^7 particles per second. The areal density of the gold targets was approximately 1 mg/cm^2.

Light particles and complex fragments were detected with the MSU Miniball phoswich detector array. For the argon beam energy of E/A=35 MeV the array covered scattering angles of Θ_{lab}=16°-160° (rings 2-11) and a solid angle corresponding to 87% of 4π. At beam energies of E/A=50, 80 and 110 MeV, the array covered scattering angles of Θ_{lab}=9°-160° (rings 1-11) and a solid angle corresponding to 89% of 4π. Details about the detector geometry are given in references [8,23,26,28].

For the $^{129}Xe+^{197}Au$ experiment the Miniball consisted of 171 detectors (rings 2-11 with 4 detectors missing from ring 2) with a solid angle coverage of approximately 87% of 4π. At very forward angles 2°-16°, fragments of charge Z=1-54 were detected with high resolution using a 16-element Si (300 μm)-Si(Li) (5 mm) - plastic (7.6 cm) array [29] with a geometrical efficiency of 64%. Where counting statistics allowed, individual atomic numbers were resolved for Z=1-54. Representative detection thresholds for fragments of Z = 2, 8, 20, and 54 fragments were approximately 6, 13, 21 and 27 MeV/nucleon. Energy

calibrations were obtained by directing 18 different beams ranging from Z=1 to 54 into each of the 16 detector elements [30]. The energy calibration of each of these detectors is accurate to better than 1%, and position resolutions of ±1.5 mm are obtained. The complete detector system subtended angles from 2°-160° with respect to the beam axis and had a geometric acceptance of > 88% of 4π.

The detector array was actively cooled and temperature stabilized. Gain drifts of the photomultiplier tubes were monitored by a light pulser system [23,28]. All events in which at least two detectors fired were recorded on magnetic tape. Random coincidences were negligible due to the low beam intensity.

Each Miniball phoswich detector consisted of a 40 μm (4 mg/cm^2) thick plastic scintillator foil backed by a 2 cm thick CsI(Tl) crystal. All detectors had aluminized mylar foils (0.15 mg/cm^2 mylar and 0.02 mg/cm^2 aluminum) placed in front of the plastic scintillator foils. As a precaution against secondary electrons, the detectors of ring 11 (Θ_{lab}=140°-160°) were covered by Pb-Sn foils of 5.05 mg/cm^2 areal density for the higher energy argon experiments (E/A=50, 80 and 110 MeV) and rings 2 and 3 were covered by aluminum foils of 0.81 mg/cm^2 for the lowest bombarding argon energy. In the xenon induced reaction, rings 9-11 of the Miniball were covered with the Pb-Sn foils. Particles punching through the 4 mg/cm^2 plastic scintillator foils were identified by atomic number up to Z=18. Hydrogen and helium were identified by isotope as well. Approximate energy thresholds are $E_{th}/A \cong 2$ MeV for Z=3, $E_{th}/A \cong 3$ MeV for Z=10 and $E_{th}/A \cong 4$ MeV for Z=18 fragments. Low energy particles stopped in the scintillator foils were recorded but could not be identified by atomic number.

Energy calibrations of forward Miniball detectors were obtained by measuring the elastic scattering of ^{4}He, ^{6}Li, ^{10}B, ^{12}C, ^{16}O, ^{20}Ne and ^{35}Cl beams

from a ^{197}Au target at incident energies of E(^{4}He)/A=4.5, 9.4, 12.9, 16 and 20 MeV; E(^{6}Li)/A=8.9 MeV; E(^{10}B)/A=15 MeV; E(^{12}C)/A=6, 8, 13 and 20 MeV; E(^{16}O)/A=16 and 20 MeV; E(^{20}Ne)/A=10.6, 11.3, 13.3, 15.0 and 19.8 MeV; and E(^{35}Cl)/A=8.8, 12.3 and 15 MeV. For detectors in rings 1-4, these calibrations are estimated to be accurate within 5%. Calibrations of more backward detectors were obtained from the energies of light particles punching through the CsI(Tl) crystals and from extrapolations of the average response of detectors at more forward angles. The resulting uncertainties in energy calibration at more backward angles are considerably larger, typically of the order of 10% and for some detectors as large as 20%.

3. Definition of impact parameter filters

For this reaction the following quantities have been used to select the magnitude of the impact parameter:

(1) The charged particle multiplicity, N_C, includes all charged particles detected by the Miniball (and the forward array for xenon-induced experiment), even if they are not identified. For example, heavy fragments stopped in the scintillator foils are included in the definition of N_C. Multiple hits in a single detector are counted as single hits even if they could be identified as multiple hits. (In many cases, the double pulse shape discrimination technique employed for the Miniball detector allows the identification of double hits. Double hits from α-particles can, for example, be clearly identified). Hence, the number N_C is equal to the number of detectors that fire on at least one charged particle.

(2) The total transverse kinetic energy of identified particles, E_t, is defined as

$$E_t = \sum_i E_i \sin^2 \theta_i = \sum_i \frac{(p_i \sin \theta_i)^2}{2m_i} . \qquad (1)$$

Here, E_i, p_i, m_i and θ_i denote the kinetic energy, momentum, mass and polar emission angle of particle i with respect to the beam axis. E_t was calculated using only the Miniball detectors.

(3) The mid-rapidity charge, Z_y, is defined [7] as the summed charge of all identified particles of rapidity y with

$$0.75y_{target}<y<0.75y_{projectile}. \quad (2)$$

All rapidities are defined in the center-of-mass frame.

As already demonstrated in ref. [8], the three observables, N_C, E_t, and Z_y, are strongly correlated. On average, an increase in the value of one observable is accompanied by an increase in the other two. As a consequence, impact parameter filters based upon any of the three observables select qualitatively similar events. For the $^{36}Ar + ^{197}Au$ reaction, the resolution of impact parameter filters based upon these three observables was found to be rather similar.

In order to construct an approximate impact parameter scale, we followed the geometrical prescription [4] utilized previously [8]. For each of the quantities N_C, E_t, and Z_y we assume a monotonic relationship to the impact parameter and define the reduced impact parameter scale

$$\frac{b(X)}{b_{max}} = \hat{b}(X) = \left(\int_X^{\infty} \frac{dP(X')}{dX'} dX' \right)^{1/2}, \quad (3)$$

where X= N_C, E_t, and Z_y; dP(X)/dX is the normalized probability distribution for the measured quantity X, and b_{max} is the maximum impact parameter for which particles were detected in the Miniball ($N_C \geq 2$). The reduced impact parameter scale $\hat{b}$ ranges from $\hat{b} = 1$ for glancing collisions to $\hat{b} = 0$ for head-on collisions.

In ref. [8] it was demonstrated that impact parameter filters based upon N_C, E_t, and Z_y were similarly effective in suppressing particles emitted with near-

projectile velocities when cuts on small reduced impact parameters were applied. While the suppression of beam velocity particles is qualitatively expected for collisions between a relatively small projectile and a relatively large target nucleus, a suppression of beam velocity fragments may not necessarily be the best indicator for event centrality. In the following section, we therefore evaluate an alternative observable which depends less on a participant-spectator picture and which is more closely related to the angular momentum effects as evidenced by an ordered motion of the emitted particles in the entrance channel reaction plane.

4. Azimuthal correlation functions

Ordered motion of the emitted particles can be detected by measurements of azimuthal correlation functions [10-16] defined by the ratio

$$\left.\frac{Y(\Delta\phi)}{Y'(\Delta\phi)}\right|_{\theta,\hat{b}} = C\left[1+R(\Delta\phi)\right]\Big|_{\theta,\hat{b}}. \qquad (4)$$

Here, $Y(\Delta\phi)$ is the coincidence yield of two (identical) particles emitted with relative azimuthal angle $\Delta\phi$ at a polar laboratory angle θ and in collisions selected by a specified cut on reduced impact parameter $\hat{b}$; $Y'(\Delta\phi)$ is the background yield constructed by mixing particle yields from different coincidence events, but selected by identical cuts on the reduced impact parameter; C is a normalization constant such that the average value of the correlation $1+R(\Delta\phi)$ is one. All azimuthal correlation functions presented in this paper were constructed from particles detected at $\theta = 31° - 50°$.

Azimuthal correlation functions may provide an additional diagnostic tool with regard to the selection of central collisions which is complementary to the suppression of beam velocity particles investigated [8] previously. For example, if projectile and target nuclei fuse at finite impact parameters, the emission of

beam velocity particles will be suppressed for all impact parameters below a certain value. However, off-center fusion reactions will induce a collective rotation of the residue. The angular velocity of this collective rotation depends on impact parameter. Particle emission from a rotating compound nucleus is focused in a plane perpendicular to the angular momentum vector, i.e. the emission will be enhanced in the reaction plane [11]. The degree of this enhancement increases with the angular velocity of rotation, and it decreases as a function of temperature. The effect becomes more pronounced for heavier emitted particles [11]. For the case of equilibrium emission from a long-lived rotating system, the emission becomes left-right symmetric and the azimuthal correlation functions exhibit a characteristic V-shape [11]. In the limit of $\hat{b} \rightarrow 0$, the collective rotation ceases and the azimuthal correlation function becomes flat, i.e. $R(\Delta\phi) \rightarrow 0$.

Nonvanishing azimuthal correlation functions have been observed in a large number of intermediate-energy heavy ion collision experiments. In many instances, slightly distorted "V"-shapes were observed [10-15] which could be understood in terms of a collective rotational motion in the reaction plane caused by the attractive mean nuclear field [19-22]. A number of other physical effects can influence the shape of the azimuthal correlation functions and lead to deviations from symmetric V-shapes. An important example is the directed transverse flow caused by the interplay of mean field deflection and pressure due to nuclear compression [1,31-34]. Additional distortions may arise from phase space constraints imposed on finite systems by momentum conservation [18,35] or final state interactions [15].

Figure 1 shows azimuthal correlation functions of protons, deuterons, tritons and He nuclei (^{3}He and ^{4}He combined) detected in peripheral ($\hat{b} > 0.75$) ^{36}Ar +

^{197}Au collisions at E/A=50 MeV. (For brevity of notation, all emitted He nuclei are denoted by the symbol α in the figures; contributions from ^{3}He are smaller than those from ^{4}He by a factor of about 5). A uniform software energy threshold of E/A=12 MeV was applied. In addition, the energies of protons, deuterons and tritons were required to be smaller than 75, 100 and 119 MeV respectively (the punch-through energies for the 2 cm thick CsI crystals). For He nuclei, no upper energy threshold was imposed since punch through He nuclei could still be cleanly identified. Consistent with previous observations for slightly different systems [10-15], the azimuthal correlation functions exhibit (slightly distorted) V-shaped patterns with a clear minimum at $\Delta\phi \approx 90°$, reflecting the known preferential emission of equilibrium as well as nonequilibrium particles in the entrance channel reaction plane [10-15,19-23]. Again consistent with previous observations [10-15,19-23], the azimuthal anisotropies become stronger with increasing mass of the particle pair. Since the effect is particularly pronounced for He nuclei and since He nuclei are emitted in great abundance, we utilize the He correlation function as a diagnostic tool for assessing whether cuts on small reduced impact parameters do, indeed, select central collisions.

5. Comparison of relative scales

Figures 2-6 show azimuthal correlation functions for He nuclei emitted in ^{36}Ar + ^{197}Au collisions at E/A = 35, 50, 80 and 110 MeV and for ^{129}Xe + ^{197}Au collisions at E/A = 50 MeV. A software threshold of E/A=8 MeV was used in selecting the He nuclei. Different panels of the figures show results for different cuts on the charged particle multiplicity N_C. For each panel, the overlapping circles present a simple geometric picture of the collision geometry deduced by means of Eq. 3. At large impact parameters, i.e. low values of N_C, the correlation functions show a strong preference of emission at relative azimuthal angles of $\Delta\phi$

$\approx 0°$ and 180°, characteristic of preferential emission in the reaction plane. At larger values of N_C, the azimuthal correlation functions become more isotropic. For a given cut on reduced impact parameter, the azimuthal correlation functions become increasingly damped as the beam energy is increased. The effect may be related to the disappearance of flow predicted and observed [31-34] in symmetric projectile-target collisions at comparable energies, possibly reflecting an increased balancing of attractive and repulsive forces from the mean nuclear field and from pressure, respectively.

In order to allow a more compact presentation of the main features of the observed azimuthal correlation functions, we have fit them by functions of the form

$$1 + \lambda_1 \cos(\Delta\phi) + \lambda_2 \cos(2\Delta\phi) \ , \qquad (5)$$

where λ_1 and λ_2 treated as free parameters. Large values of λ_2 may be associated with collective motion resembling a rotation [36]. Positive (negative) values of λ_1 indicate preferential emission of the particle pair to the same side (opposite sides) of the beam. Positive values of λ_1 can come from large final state interactions (e.g. the decay $^8Be \rightarrow 2\alpha$) or, alternatively, from directed sideward flow. Negative values of λ_1 (preferred emission on opposite sides of the beam) may reflect phase space constraints for small systems due to momentum conservation [18,35]. For isotropic distributions $\lambda_1=\lambda_2=0$.

Figure 7 summarizes the parameters, λ_1 and λ_2, extracted as a function of reduced impact parameter $\hat{b}(N_C)$ for $^{36}Ar + ^{197}Au$ collisions at the different bombarding energies. At all bombarding energies, λ_2 decreases as a function of decreasing reduced impact parameter. Indeed, for $E/A \geq 50$ MeV, $\lambda_2 \rightarrow 0$ as $\hat{b}(N_C) \rightarrow 0$ with rather good accuracy, indicating that small reduced impact parameters do, indeed, select near-central collisions for which $R(\Delta\phi) \approx 0$ by

necessity. At E/A=35 MeV, the selection of central collisions appears to be of slightly reduced quality since $\lambda_2 \geq 0.1$ even for very small values of $\hat{b}(N_C)$. To some extent, reduced selectivity for very central collisions at the lower energy may result from a loss of statistical resolution as $\Delta N_C/N_C$ becomes larger at lower incident energy. It is more likely, however, that this loss of resolution is related to the breakdown of the participant-spectator picture which underlies impact parameter filters measuring the "violence" of the collision.

As expected from the qualitative trends apparent in Figs. 2-6, the values of λ_2 at fixed $\hat{b}(N_C)$ are largest for the lowest bombarding energy where rotational deflection of the emitted particles by the mean nuclear fields is most pronounced. At E/A=50, 80 and 110 MeV, λ_1 is nearly zero for reduced impact parameters $\hat{b}(N_C) < 0.4$. For larger reduced impact parameters, as well as for E/A=35 MeV, λ_1 assumes small but positive values. Positive values of λ_1 may indicate a weak sideward directed flow, but they can also arise from the sequential decay of particle unstable nuclei, in this case ^{8}Be.

In order to discern between these two possibilities, we show in Figs. 8 and 9 the parameters λ_1 and λ_2 which characterize the azimuthal correlations of protons, deuterons, tritons and He nuclei emitted in ^{36}Ar + ^{197}Au and ^{129}Xe + ^{197}Au collisions, respectively, at E/A = 50 MeV. The clear monotonic dependence of the extracted values of λ_2 on the mass of the detected particle pair (top panel)s illustrates the well known fact [11] that collective effects are most readily discerned in the emission patterns of heavy particles. In contrast, the parameters λ_1 do not exhibit a monotonic mass dependence. At large impact parameters, the extracted values of λ_1 are consistent with zero for protons, they assume small negative values for deuterons and tritons and small positive values for He nuclei.

Most likely, the small negative and positive values of λ_1 reflect distortions due to final state interactions (possibly modified by additional momentum conservation effects [18]). Indeed, the changes in sign of λ_1 follow the qualitative differences of the final state interactions which determine the shapes of small angle correlation functions of these particles, see e.g. ref. [17]. For pairs of deuterons and tritons, correlations at small relative momenta are suppressed [17]. For these particles, the final state interaction is dominated by the repulsive Coulomb interaction, since there are no contributions from low lying resonances. For α-particles, on the other hand, correlations at small relative momenta are strongly enhanced due to large contributions from the decay of ^{8}Be [17]. The case of two-proton correlations lies in between: here the correlation function exhibits a minimum at very small relative momenta followed by a broad maximum at relative momentum 20 MeV/c [17]. For the present data, a quantitative interpretation of the parameter λ_1 solely in terms of collective flow effects appears inappropriate, and final state interactions or other many-body correlations may have to be considered. Since these effects are of little interest in the context of the present paper, we do not pursue this issue further.

Figures 10 and 11 show that impact parameter filters based upon N_C, E_t, and Z_Y select, as expected [8], classes of events characterized by very similar azimuthal distributions. The figures show the reduced-impact-parameter dependence of the parameters λ_1 and λ_2 which characterize the azimuthal correlations functions of He nuclei emitted in ^{36}Ar + ^{197}Au and ^{129}Xe + ^{197}Au reactions at E/A = 50 MeV. The different symbols in the figures indicate the use of different impact parameter filters, $\hat{b}(N_C)$ (solid circles), $\hat{b}(E_t)$ (open circles), and $\hat{b}(Z_Y)$ (solid diamonds). As determined from to the shape of azimuthal correlation functions, the three impact parameter scales provide equivalent event

selection. Only for the most peripheral reactions, some slight differences exist. Small discrepancies between different impact parameter filters for peripheral collisions are not surprising since the determination of large impact parameters must be associated with relatively large statistical and systematic uncertainties. The present findings are qualitatively consistent with the results of ref. [8].

6. Directivity

For intermediate energy nucleus-nucleus collisions, the highest degree of equilibration is expected to occur in central collisions. Investigations of the thermodynamic properties of nuclear matter should therefore be performed with reaction filters optimized to provide high selectivity of very small impact parameters. Recently an improved method for the selection of central collisions was suggested [9] which employed simultaneous cuts on large charged-particle multiplicities and small transverse-momentum directivities. The experimental evidence for improved selectivity of small impact parameters was based upon data at significantly higher incident energy and with experimental apparatus of restricted solid angle coverage ($\theta_{lab} < 30°$). In this section we explore whether similar improvements in small-impact-parameter selectivity can be obtained for the present data taken at lower beam energies and with more complete solid angle coverage.

The transverse-momentum directivity D is defined as

$$D = \left\{ \frac{\left| \sum_i \mathbf{p}_i^{\perp} \right|}{\sum_i \left| \mathbf{p}_i^{\perp} \right|} \right\}_{Y_i \geq Y_{cm}} . \qquad (6)$$

In Eq. 6, the sum includes all identified particles with rapidities larger than the center-of-mass rapidity, and $\mathbf{p}_i^{\perp}$ denotes the transverse momentum of detected particle i. The momenta are calculated assuming A=2Z for $3 \leq Z \leq 18$.

Following the procedure outlined in ref. [9], we explored the conditional distribution of impact parameters $\hat{b}(E_t)$ selected by the cuts $\hat{b}(N_C) = 0.05 - 0.1$ and $D \leq 0.2$. The results are shown in Fig. 12. The dashed and dotted-dashed lines show the results for cuts on $\hat{b}(N_C)$ and D only, and the solid line shows the results for a simultaneous cut on $\hat{b}(N_C)$ and D. A single cut on D alone provides little selectivity of central collisions, and no improvement in the $\hat{b}(E_t)$-distribution is observed if an additional cut on D<0.2 is imposed beyond the cut $\hat{b}(N_C) = 0.05 - 0.1$. This insensitivity to additional cuts on D should be compared to that observed for other impact parameter filters, based for example on the mid-rapidity charge Z_Y: narrower $\hat{b}(E_t)$-distributions were obtained when double cuts on N_C and Z_Y were employed [8]. We conclude that cuts on directivity provide little additional selectively, at least for the present set of data taken at lower energy and with full 4π-coverage.

Cuts on small values of the transverse-momentum directivity suppress collisions which exhibit significant transverse flow. Hence, such cuts are ineffective in systems for which transverse flow is small or negligible. Indeed, for the reactions investigated here, small values of λ_1 were extracted from the azimuthal distributions, and these small values could not be associated with transverse flow effects. The dashed curve in Fig. 13 shows the distribution in transverse momentum directivity for $^{36}Ar + ^{197}Au$ collisions at E/A=110 MeV selected by a cut on small reduced impact parameters, $\hat{b}(N_C) \leq 0.2$. For comparison, the solid curve shows the distribution for the same set of events after randomization of the azimuthal emission angles, i.e. after an artificial

elimination of any existing flow effects. The true experimental distribution and the randomized distribution are very similar. In particular, the experimental distributions does not exhibit an excessive tail towards larger values of D which could be eliminated by cuts on small values of D. For the present reactions, additional cuts on transverse directivity do not enhance the selectivity of central collisions beyond that achieved by tight cuts on small reduced impact parameters. The success of applying cuts on the transverse directivity at higher energies [9] may be due to the presence of larger transverse flow effects at these energies, and partly due to a relatively poor impact parameter selection by multiplicity filters which only cover part of the full solid angle [1,37].

7. Summary

In this paper, we explored the effect of impact parameter filters based upon the detected charged particle multiplicity N_C, the transverse energy E_t, and the midrapidity charge Z_Y on the azimuthal correlation function between emitted light particles. Azimuthal correlations functions are sensitive to the presence of collective velocity components in the reaction plane. In many reaction scenarios the ordered motion in the reaction plane depends upon the angular momentum of the emitting system and, hence, upon impact parameter. This impact parameter dependence is complementary to quantities which provide a measure of the geometric overlap of projectile and target nuclei as for example the relative intensity of emission from a projectile-like source explored in our previous investigation of impact parameter filters [8].

As was done in ref. [8], we employed a simple geometric prescription for the construction of reduced impact parameter scales based upon the observables (N_C, E_t, and Z_Y) to provide a quantitative basis for the comparison of these

different impact parameter filters. For the reactions studied in this paper, these reduced impact parameter scales were found to select classes of events with very similar azimuthal correlation functions. At large reduced impact parameters, the azimuthal correlation functions exhibit strong anisotropies indicating preferred emission in the reaction plane. At small reduced impact parameters, the correlations are nearly flat indicating isotropic emission. This evolution of the azimuthal correlation functions as a function of reduced impact parameter is consistent with the expected dependence on the true impact parameter of the reaction. For the reactions investigated in this paper, cuts on small reduced impact parameters were found to be effective in selecting central or near-central collisions, and no additional selectivity for central collisions was found by imposing additional cuts on transverse momentum directivity.

This work was supported by the National Science Foundation under Grant No. PHY-9214992.

References.

1. M.B. Tsang, G.F. Bertsch, W.G. Lynch and M. Tohyama, Phys. Rev. C **40** (1989) 1685.
2. R. Stock, Phys. Reports **135** (1986) 259.
3. H. Stöcker and W. Greiner, Phys. Reports **137**, (1986) 277.
4. C. Cavata, M. Demoulins, J. Gosset, M.C. Lemaire, D. L'Hôte, J. Poitou and O. Valette, Phys. Rev. C **42** (1990) 1760.
5. H.G. Ritter, Nucl. Phys. **A488** (1988) 651c.
6. J. Hubele, P. Kreutz, J.C. Adloff, M. Begemann-Blaich, P. Bouisson, G. Imme, I. Iori, G.J. Kunde, S. Leray, V. Lindenstruth, Z. Liu, U. Lynen, R.H. Meijer, U. Milkau, A. Moroni, W.F.J. Müller, C. Ngô, C.A. Ogilvie, J. Pochodzalla, G. Raciti, G. Rudolf, H. Sann, A. Schüttauf, W. Seidel, L. Stugge, W. Trautmann, and A. Tucholski, Z. Phys. **A340** (1991) 263.
7. C.A. Ogilvie, D. Cebra, J. Clayton, S. Howden, J. Karn, A. Vander Molen, G.D. Westfall, W.K. Wilson and J.S. Winfield, Phys. Rev. C **40** (1989) 654.
8. L. Phair, D.R. Bowman, C.K. Gelbke, W.G. Gong, Y.D. Kim, M.A. Lisa, W.G. Lynch G.F. Peaslee, R.T. de Souza, M.B. Tsang and F. Zhu, Nucl. Phys. **A458** (1992) 489.
9. J.P. Alard, Z. Basrak, N. Bastid, I.M. Belayev, M. Bini, Th. Blaich, R. Bock, A. Buta, R. Caplar, C. Cerruti, N. Cindro, J.P. Coffin, M. Crouau, P. Dupieux, J. Erö, Z.G. Fan, P. Fintz, Z. Fodor, R. Freifelder, L. Fraysse, S. Frolov, A. Gobbi, Y. Grigorian, G. Guillaume, N. Gerrmann, K.D. Hildenbrand, S. Hölbling, O. Houari, S.C. Jeong, M. Jorio, F. Jundt, J. Kecskemeti, P. Koncz, Y. Korchagin, R. Kotte, M. Krämer, C. Kuhn, I. Legrand, A. Lebedev, C. Maguire, V. Manko, T. Matulewicz, G. Mgebrishvili, J. Mösner, D. Moisa, G. Montarou, P. Morel, W. Neubert, A. Olmi, G. Pasquali, D. Pelte, M. Petrovici, G. Poggi, F. Rami, W. Reisdorf, A. Sadchikov, D. Schüll, Z. Seres, B. Sikora, V. Simion, S. Smolyankin, U. Sodan, N. Taccetti, K. Teh, R. Tezkratt, M. Trzaska, M.A. Vasiliev, P. Wagner, J.P. Wessels, T. Wienold, Z. Wilhelmi, D. Wohlfarth, and A.V. Zhilin, Phys. Rev. Lett. **69** (1992) 889.

10. M.B. Tsang, W.G. Lynch, C.B. Chitwood, D.J. Fields, D.R. Klesch, C.K. Gelbke, G.R. Young, T.C. Awes, R.L. Ferguson, F.E. Obenshain, F. Plasil and R.L. Robinson, Phys. Lett. B **148**, (1984) 265.

11. C.B. Chitwood, D.J. Fields, C.K. Gelbke, D.R. Klesch, W.G. Lynch, M.B. Tsang, T.C. Awes, R.L. Ferguson, F.E. Obenshain, F. Plasil, R.L. Robinson, and G.R. Young, Phys. Rev. **C34** (1986) 858.

12. D.J. Fields, W.G. Lynch, T.K. Nayak, M.B. Tsang, C.B. Chitwood, C.K. Gelbke, R. Morse, J. Wilczynski, T.C. Awes, R.L. Ferguson, F. Plasil, F.E. Obenshain, and G.R. Young, Phys. Rev. **C34** (1986) 536.

13. M.B. Tsang, Y.D. Kim, N. Carlin, Z. Chen, C.K. Gelbke, W.G. Gong, W.G. Lynch, T. Murakami, T. Nayak, R.M. Ronningen, H.M. Xu, F. Zhu, L.G. Sobotka, D.W. Stracener, D.G. Sarantites, Z. Majka, and V. Abenante, Phys. Rev. **C42** (1990) R15.

14. D. Ardouin, Z. Basrak, P. Schuck, A. Péghaire, F. Saint-Laurent, H. Delagrange, H. Doubre, C. Grégoire, A. Kyanowski, W. Mittig, J. Péter, Y.P. Viyogi, J. Québert, C.K. Gelbke, W.G. Lynch, M. Maier, J. Pochodzalla, G. Bizard, F. Lefèbvres, B. Tamain, B. Remaud, and F. Sébille, Nucl. Phys. **A514** (1990) 564.

15. A. Elmaani, N.N. Ajitanand, J.M. Alexander, R. Lacey, S. Kox, E. Liatard, F. Merchez, T. Motobayashi, B. Noren, C. Perrin, D. Rebreyend, T.U. Chan, G. Anges, and S. Groult, Phys. Rev. **C43** (1991) R2474.

16. S. Wang, Y.Z. Jiang, Y.M. Liu, D. Keane, D. Beavis, S.Y. Chu, S.Y. Fung, M. Vient, C. Hartnack and H. Stöcker Phys. Rev. C **44** (1991) 1091.

17. J. Pochodzalla, C.K. Gelbke, W.G. Lynch, M. Maier, D. Ardouin, H. Delagrange, H. Doubre, C. Grégoire, A. Kyanowski, W. Mittig, A. Péghaire, J. Péter, F. Saint-Laurent, B. Zwieglinski, G. Bizard, F. Lefèbvres, B. Tamain, and J. Québert, Y.P. Viyogi, W.A. Friedman, and D.H. Boal, Phys. Rev. **C35** (1987) 1695.

18. W.G. Lynch, L.W. Richardson, M.B. Tsang, R.E. Ellis, C.K. Gelbke and R.E. Warner, Phys. Lett. **108B** (1982) 274.

19. M.B. Tsang, C.B. Chitwood, D.J. Fields, C.K. Gelbke, D.R. Klesch, W.G. Lynch, K. Kwiatkowski and V.E. Viola, Jr., Phys. Rev. Lett. **52** (1984) 1967.

20. M.B. Tsang, R.M. Ronningen, G. Bertsch, Z. Chen, C.B. Chitwood, D.J. Fields, C.K. Gelbke, W.G. Lynch, T. Nayak, J. Pochodzalla, T. Shea, and W. Trautmann, Phys. Rev. Lett. **57** (1986) 559.

21. M.B. Tsang, W.G. Lynch, R.M. Ronningen, Z. Chen, C.K. Gelbke, T. Nayak, J. Pochodzalla, F. Zhu, M. Tohyama, W. Trautmann, and W. Dünnweber, Phys. Rev. Lett. **60** (1988) 1479.

22. W.K. Wilson, W. Benenson, D.A. Cebra, J. Clayton, S. Howden, J. Karn, T. Li, C.A. Ogilvie, A. Vander Molen, G.D. Westfall, J.S. Winfield, and A. Nadasen, Phys. Rev. **C41** (1990) R1881.

23. M.B. Tsang, R.T. de Souza, Y.D. Kim, D.R. Bowman, N. Carlin, C.K. Gelbke, W.G. Gong, W.G. Lynch, L. Phair and F. Zhu, Phys. Rev. **C44** (1991) 2065.

24. D.R. Bowman, G.F. Peaslee, R.T. de Souza, N. Carlin, C.K. Gelbke, W.G. Gong, Y.D. Kim, M.A. Lisa, W.G. Lynch, L. Phair, M.B. Tsang, C. Williams, N. Colonna, K. Hanold, M.A. McMahan, G.J. Wozniak, L.G. Moretto, and W.A. Friedman, Phys. Rev. Lett. **67** (1991) 1527.

25. R.T. de Souza, L. Phair, D.R. Bowman, N. Carlin, C.K. Gelbke, W.G. Gong, Y.D. Kim, M.A. Lisa, W.G. Lynch, G.F. Peaslee, M.B. Tsang, H.M. Xu, F. Zhu, and W.A. Friedman, Phys. Lett. **B268** (1991) 6.

26. Y.D. Kim, R.T. de Souza, D.R. Bowman, N. Carlin, C.K. Gelbke, W.G. Gong, W.G. Lynch, L. Phair, M.B. Tsang, and F. Zhu, Phys. Rev. **C45** (1992) 338.

27. D.R. Bowman, C.M. Mader, G.F. Peaslee, W. Bauer, N. Carlin, R.T. de Souza, C.K. Gelbke, W.G. Gong, Y.D. Kim, M.A. Lisa, W.G. Lynch, L. Phair, M.B. Tsang, C. Williams, N. Colonna, K. Hanold, M.A. McMahan, G.J. Wozniak, L.G. Moretto, and W.A. Friedman, Phys. Rev. **C46** (1992) 1834.

28. R.T. de Souza, N. Carlin, Y.D. Kim, J. Ottarson, L. Phair, D.R. Bowman, C.K. Gelbke, W.G. Gong, W.G. Lynch, R.A. Pelak, T. Peterson, G. Poggi, M.B. Tsang and H.M. Xu, Nucl. Instr. Meth. **A295** (1990) 109.

29. W.L. Kehoe, A.C. Mignerey, A. Moroni, I. Iori, G.F. Peaslee, N. Colonna, K. Hanold, D.R. Bowman, L.G. Moretto, M.A. McMahan, J.T. Walton, and G.J. Wozniak, Nucl. Instr. Meth. A **311** (1992) 258.

30. M.A. McMahan, G.J. Wozniak, C.M. Lyneis, D.R. Bowman, R.J. Charity, Z.H. Liu, L.G. Moretto, A.C. Mignerey and M.N. Namboodiri, Nucl. Instr. Meth. A **253** (1986) 1.

31. J.J. Molitoris and H. Stöcker, Phys. Lett. **162B** (1985) 47.

32. C.A. Ogilvie, W. Bauer, D.A. Cebra, J. Clayton, S. Howden, J. Karn, A. Nadasen, A. Vander Molen, G.D. Westfall, W.K. Wilson, and J.S. Winfield, Phys. Rev. **C42** (1990) R10.

33. W.K. Wilson, W. Benenson, D.A. Cebra, J. Clayton, S. Howden, J. Karn, T. Li, C.A. Ogilvie, A. Vander Molen, G.D. Westfall, J.S. Winfield, B. Young, and A. Nadasen, Phys. Rev. **C41** (1990) R1881.

34. J.P. Sullivan, J. Péter, D. Cussol, G. Bizard, P. Brou, M. Louvel, J.P. Patry, R. Regimbart, J.C. Steckmeyer, B. Tamain, E. Crema, H. Doubre, K. Hagel, G.M. Jin, A. Péghaire, F. Saint-Laurent, Y. Cassagnou, R. Legrain, C. Lebrun, E. Rosato, R. McGrath, S.C. Jeong, S.M. Lee, Y. Nagashima, T. Nakagawa, M. Ogihara, J, Kasagi, and T. Motobayashi, Phys. Lett. **B249** (1990) 8.

35. C.A. Ogilvie, D.A. Cebra, J. Clayton, P. Danielewicz, S. Howden, J. Karn, A. Nadasen, A. Vander Molen, G.D. Westfall, W.K. Wilson, and J.S. Winfield, Phys. Rev. **C40** (1989) 2592.

36. R. Lacey, A. Elmaani, J. Lauret, T. Li, W. Bauer, D. Craig, M. Cronqvist, E. Gualtieri, S. Hannuschke, T. Reposeur, A. Vander Molen, G.D. Westfall, W.K. Wilson, J.S. Winfield, J. Yee, S. Yennello, A. Nadasen, R.S. Tickle, and E. Norbeck, Phys. Rev. Lett. **70** (1993) 1224.

37. M.B. Tsang, Y.D. Kim, N. Carlin, Z. Chen, R. Fox, C.K. Gelbke, W.G. Gong, W.G. Lynch, T. Murakami, T.K. Nayak, R.M. Ronningen, H.M. Xu, F. Zhu, L. Sobotka, D. Stracener, D.G. Sarantites, Z. Majka, V. Abenante, and H. Griffin, Phys. Lett. **B220** (1989) 492.

Figure Captions:

Fig. 1: Azimuthal correlation functions constructed from particle pairs of protons, deuterons, tritons and He nuclei emitted in peripheral $^{36}Ar + ^{197}Au$ collisions ($\hat{b} > 0.75$, N_C = 2-9) at E/A=50 MeV. The correlation functions were constructed for particles emitted at polar angles of θ_{lab} = 31°-50° using an energy threshold E_{th}/A = 12 MeV.

Fig. 2: Azimuthal correlation functions for He nuclei emitted in $^{36}Ar + ^{197}Au$ collisions at E/A = 35 MeV. Panels from left to right show data selected by cuts on reduced impact parameters $\hat{b}$ = 0.8, 0.6, 0.4, and <0.2, respectively; the actual cuts on charged particle multiplicity N_C are indicated in the figure. The circles show the approximate geometrical overlap between target and projectile for the different cuts in N_C.

Fig. 3: As fig. 2, for E/A = 50 MeV.

Fig. 4: As fig. 2, for E/A = 80 MeV.

Fig. 5: As fig. 2, for E/A = 110 MeV.

Fig. 6: Azimuthal correlation functions for He nuclei emitted in $^{129}Xe + ^{197}Au$ collisions at E/A = 50 MeV. Panels from left to right show data selected by cuts on reduced impact parameters $\hat{b}$ = 0.8, 0.6, 0.4, and <0.2, respectively; the actual cuts on charged particle multiplicity N_C are indicated in the figure. The circles show the approximate geometrical overlap between target and projectile for the different cuts in N_C.

Fig. 7: Reduced-impact-parameter dependence of the coefficients λ_1 and λ_2 used to fit the measured azimuthal correlation functions for emitted He nuclei emitted in $^{36}Ar + ^{197}Au$ collisions at E/A = 35, 50, 80, and 110 MeV.

Fig. 8: Reduced-impact-parameter dependence of the coefficients λ_1 and λ_2 used to fit the measured azimuthal correlation functions of protons, deuterons, tritons or He-nuclei emitted in $^{36}Ar + ^{197}Au$ collisions at E/A = 50 MeV.

Fig. 9: Reduced-impact-parameter dependence of the coefficients λ_1 and λ_2 used to fit the measured azimuthal correlation functions of protons, deuterons, tritons or He-nuclei emitted in $^{129}Xe + ^{197}Au$ collisions at E/A = 50 MeV.

Fig. 10: Reduced-impact-parameter dependence of the coefficients λ_1 and λ_2 used to fit the measured azimuthal correlation functions of He-nuclei emitted in $^{36}Ar + ^{197}Au$ collisions at E/A = 50 MeV. Results from different impact parameters filters are shown by the different symbols indicated in the figure.

Fig. 11: Reduced-impact-parameter dependence of the coefficients λ_1 and λ_2 used to fit the measured azimuthal correlation functions of He-nuclei emitted in $^{129}Xe + ^{197}Au$ collisions at E/A = 50 MeV. Results from different impact parameters filters are shown by the different symbols indicated in the figure.

Fig. 12: Conditional impact parameter distributions, $dP\left[\hat{b}(E_t)\right] / d\hat{b}(E_t)$, for $^{36}Ar + ^{197}Au$ collisions at E/A = 110 MeV selected by cuts on $\hat{b}(N_C) = 0.05 - 0.1$ (dashed curve), directivity $D \leq 0.2$ (dotted-dashed curve), and for the simultaneous cuts $\hat{b}(N_C) = 0.05 - 0.1$ and $D \leq 0.2$ (solid curve).

Fig. 13: Distribution of transverse momentum directivity D for $^{36}Ar + ^{197}Au$ collisions at E/A = 110 MeV selected by cuts on $\hat{b}(N_C) < 0.2$ (dashed curve). The solid curve shows the distribution of the transverse momentum directivity obtained after randomizing the azimuthal distribution of the emitted particles according to an isotropic distribution (solid curve).

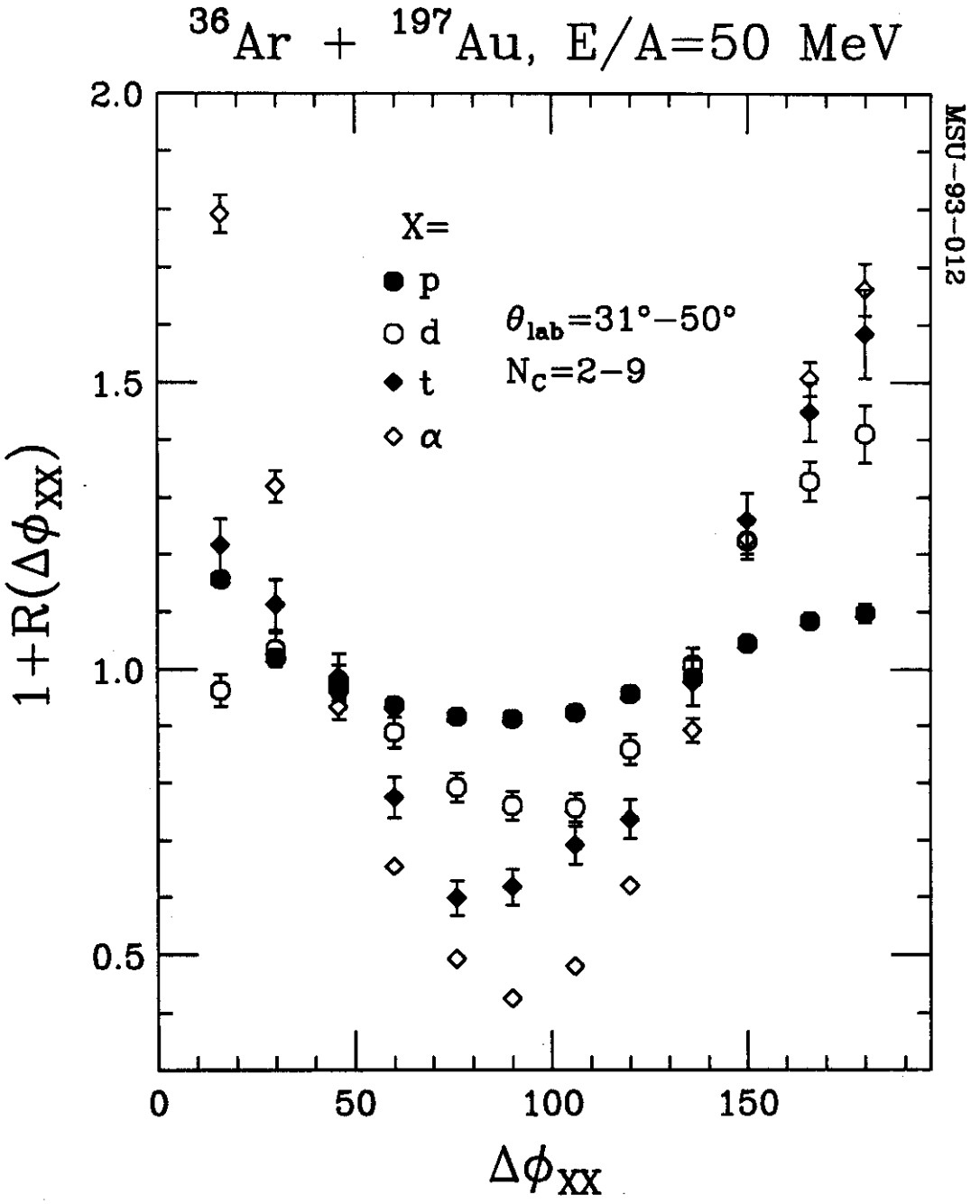
^{36}Ar + ^{197}Au, E/A=50 MeV
MSU-93-012
X=
p
d
t
α
θ_{lab}=31°–50°
N_C=2–9
1+R($\Delta\phi_{XX}$)
$\Delta\phi_{XX}$
2.0
1.5
1.0
0.5
0
50
100
150

Fig. 1

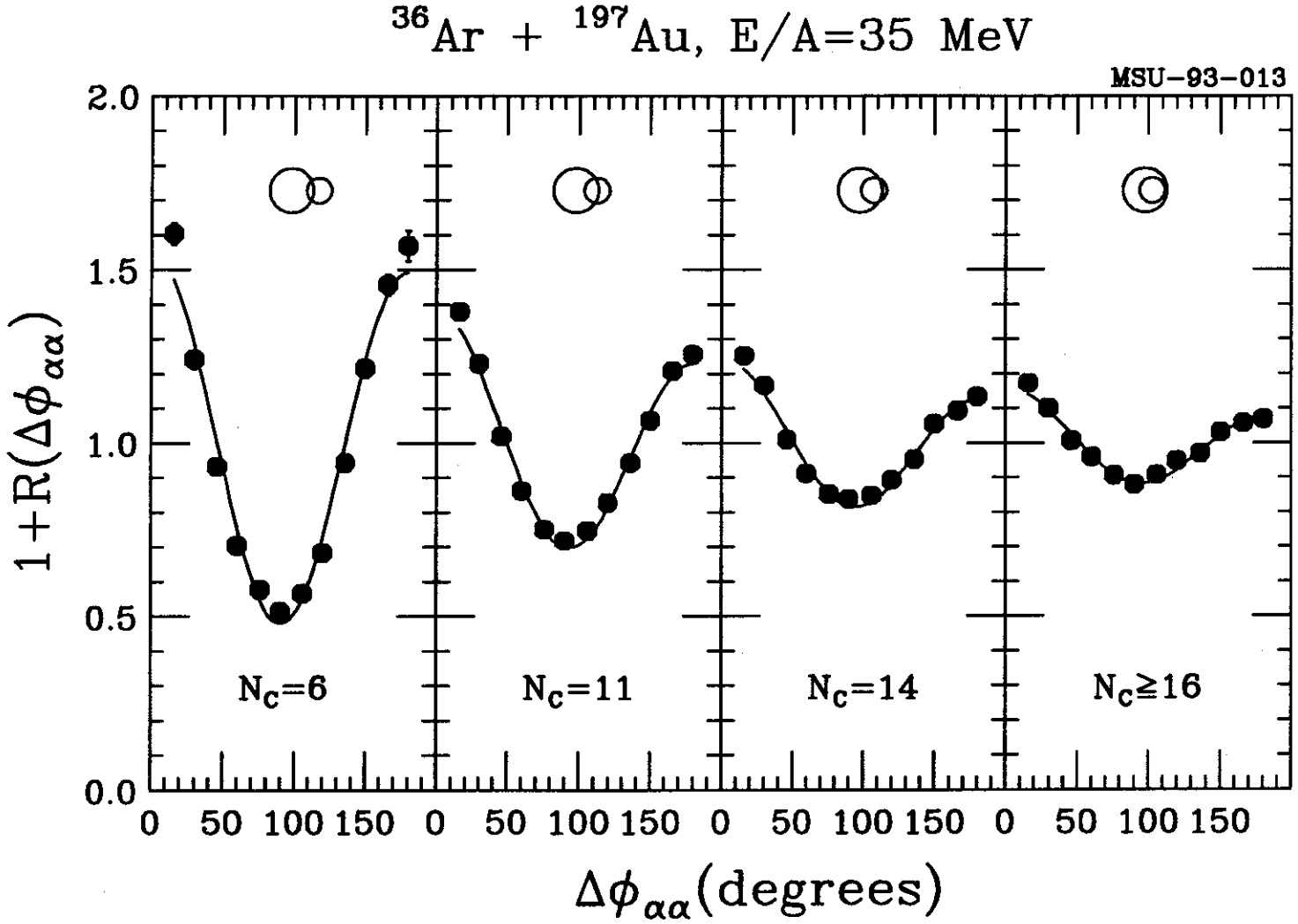
^{36}Ar + ^{197}Au, E/A=35 MeV
MSU-93-013
2.0
1.5
1.0
0.5
0.0
1+R($\Delta\phi_{\alpha\alpha}$)
N_c=6
N_c=11
N_c=14
$N_c\geq$16
0 50 100 150 0 50 100 150 0 50 100 150 0 50 100 150
$\Delta\phi_{\alpha\alpha}$(degrees)

Fig. 2

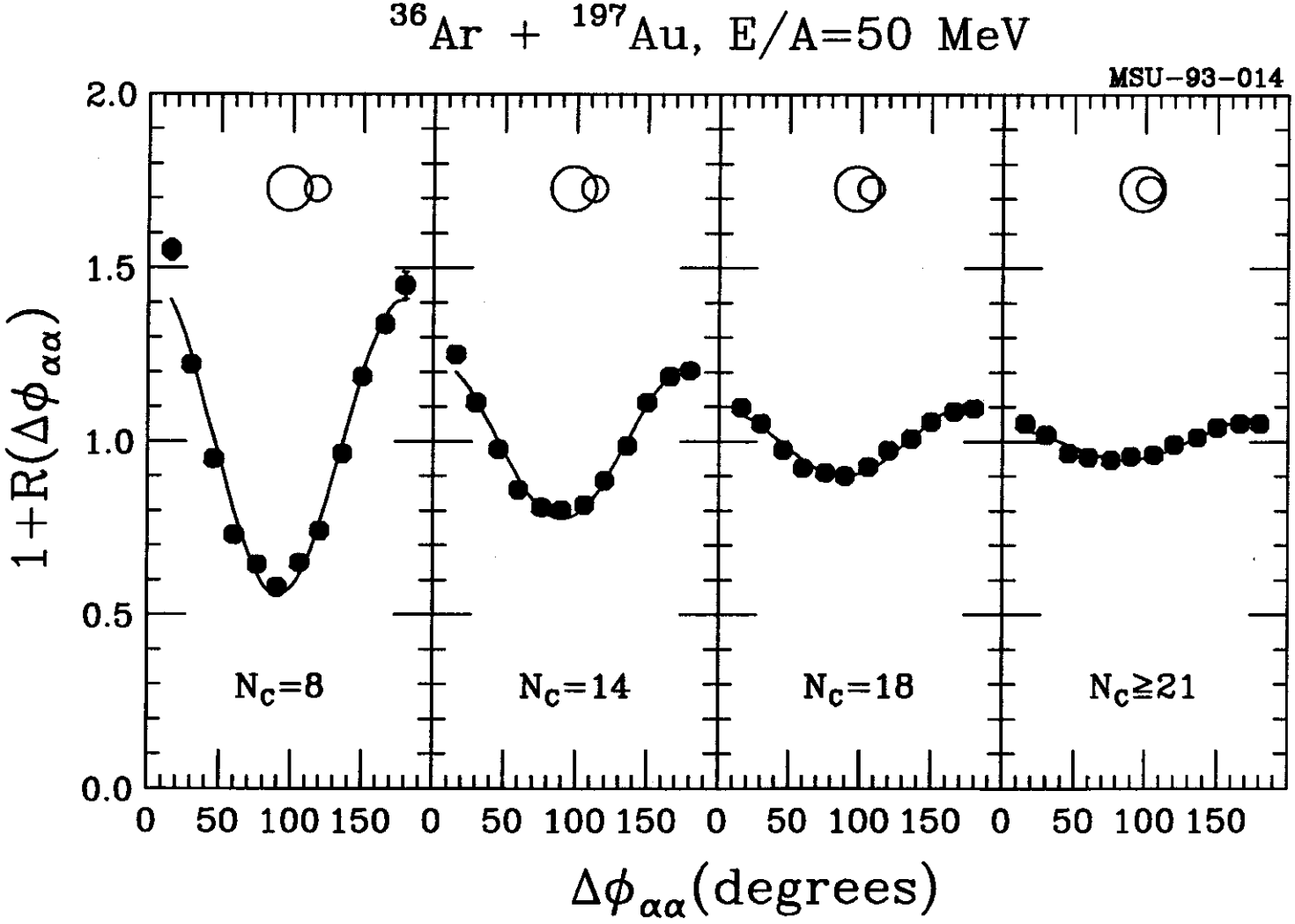
^{36}Ar + ^{197}Au, E/A=50 MeV
MSU-93-014
2.0
1.5
1.0
0.5
0.0
1+R($\Delta\phi_{\alpha\alpha}$)
N_c=8
N_c=14
N_c=18
N_c≧21
0 50 100 150 0 50 100 150 0 50 100 150 0 50 100 150
$\Delta\phi_{\alpha\alpha}$(degrees)

Fig. 3

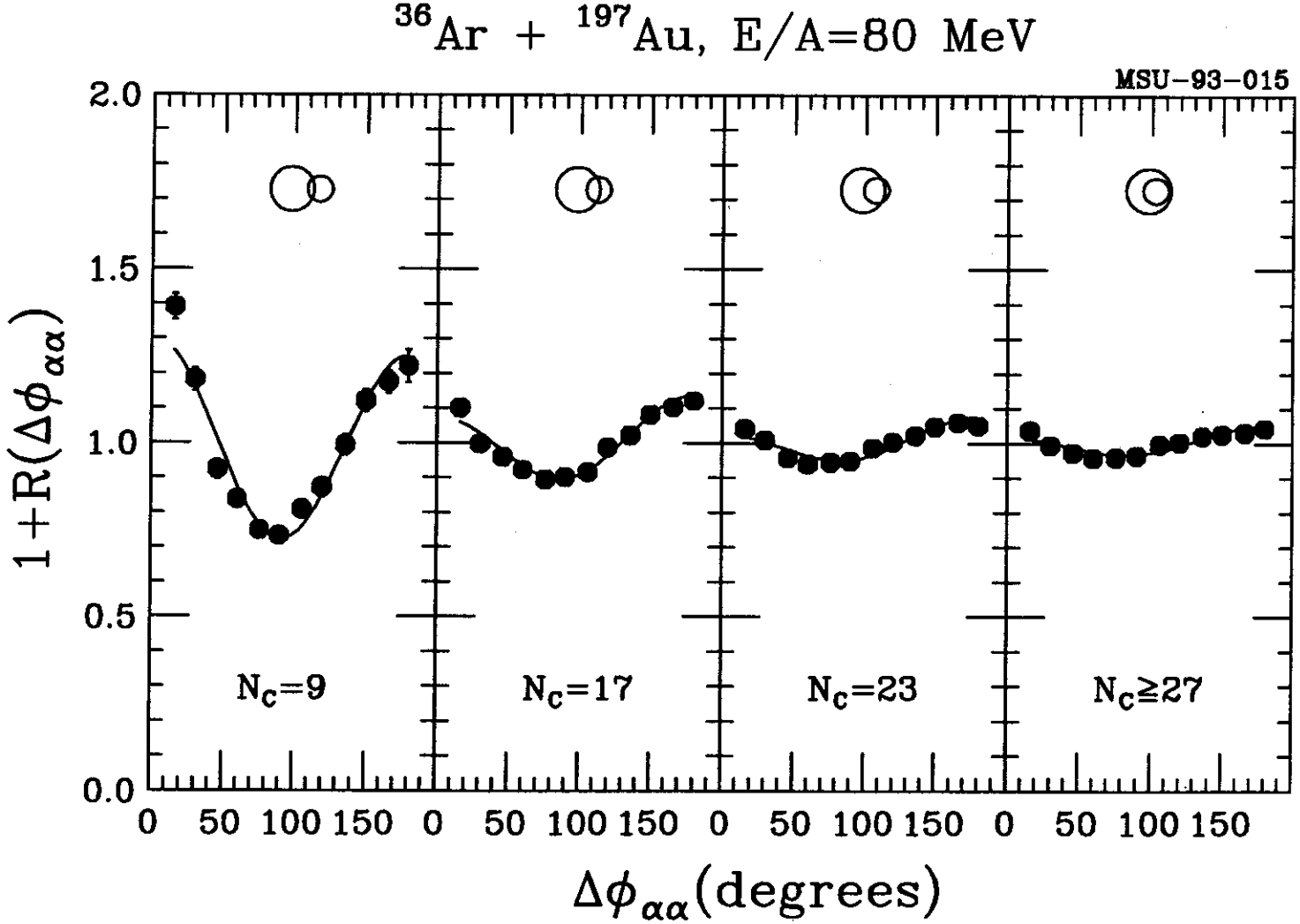
^{36}Ar + ^{197}Au, E/A=80 MeV
MSU-93-015
2.0
1.5
1.0
0.5
0.0
1+R($\Delta\phi_{\alpha\alpha}$)
N_c=9
N_c=17
N_c=23
$N_c\geq$27
0 50 100 150 0 50 100 150 0 50 100 150 0 50 100 150
$\Delta\phi_{\alpha\alpha}$(degrees)

Fig 4

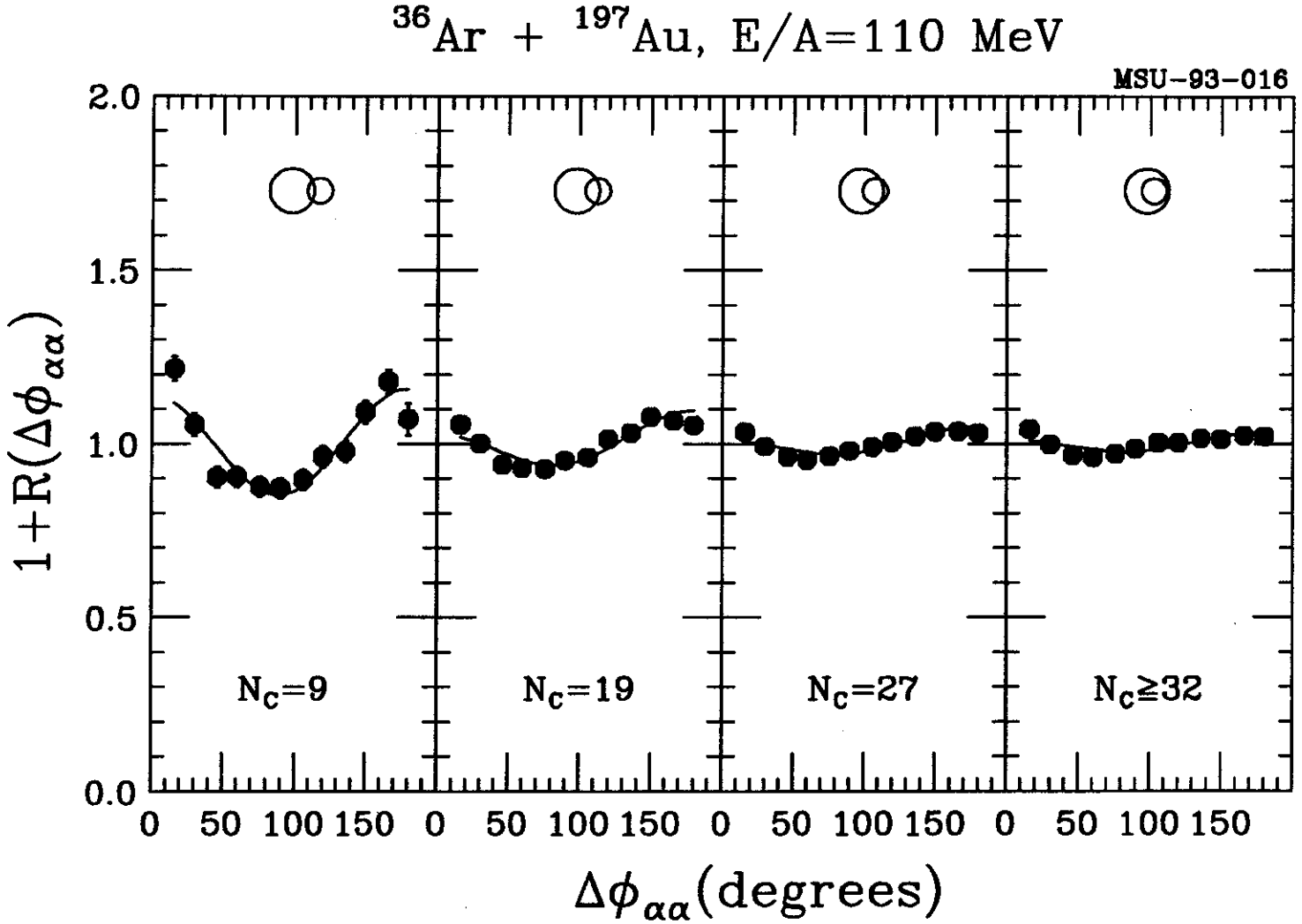
^{36}Ar + ^{197}Au, E/A=110 MeV
MSU-93-016
2.0
1.5
1.0
0.5
0.0
1+R($\Delta\phi_{\alpha\alpha}$)
N_c=9
N_c=19
N_c=27
N_c≧32
0 50 100 150 0 50 100 150 0 50 100 150 0 50 100 150
$\Delta\phi_{\alpha\alpha}$(degrees)

Fig 5

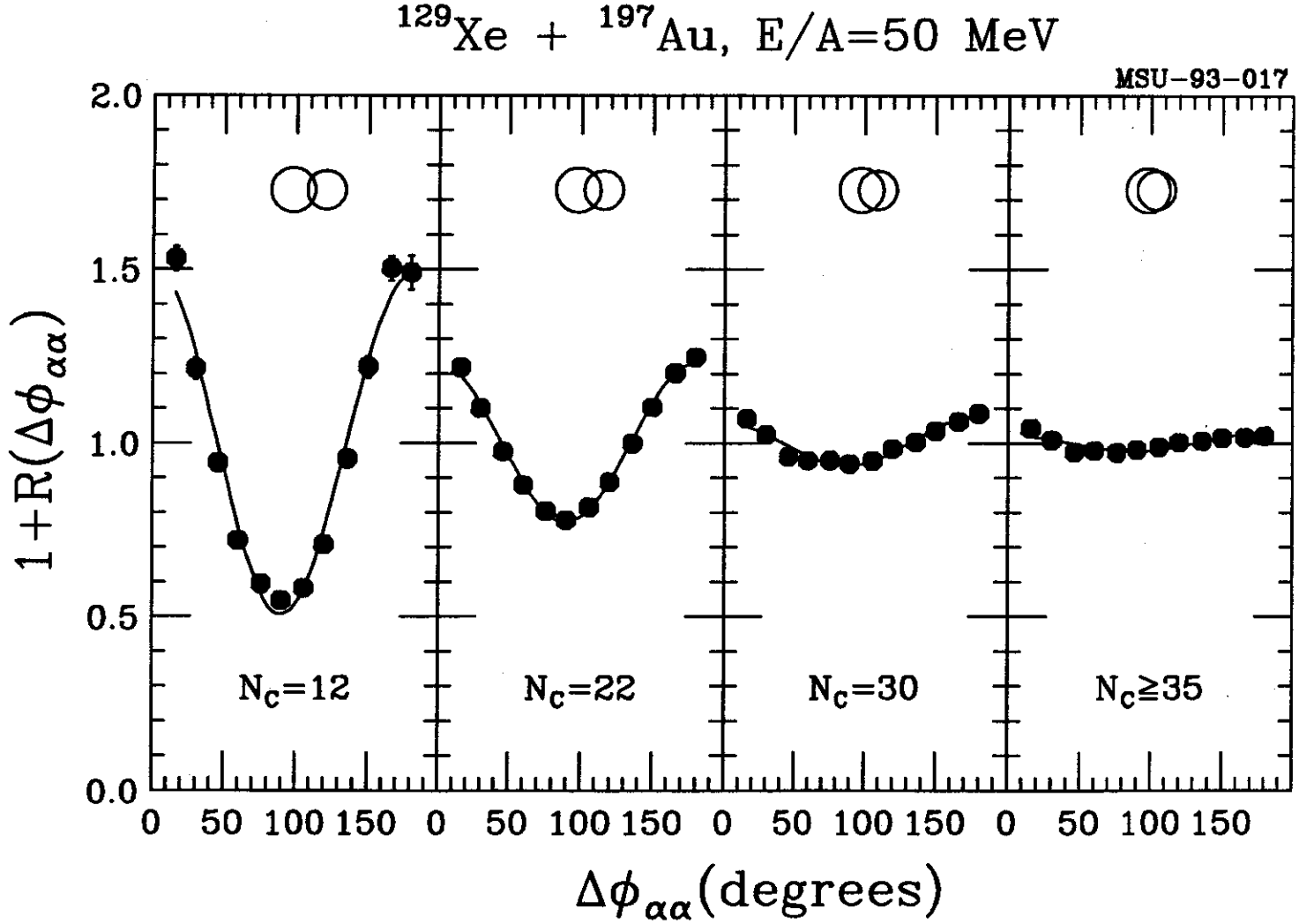
^{129}Xe + ^{197}Au, E/A=50 MeV
MSU-93-017
2.0
1.5
1.0
0.5
0.0
1+R($\Delta\phi_{\alpha\alpha}$)
N_c=12
N_c=22
N_c=30
N_c≧35
0 50 100 150 0 50 100 150 0 50 100 150 0 50 100 150
$\Delta\phi_{\alpha\alpha}$(degrees)

Fig. 6

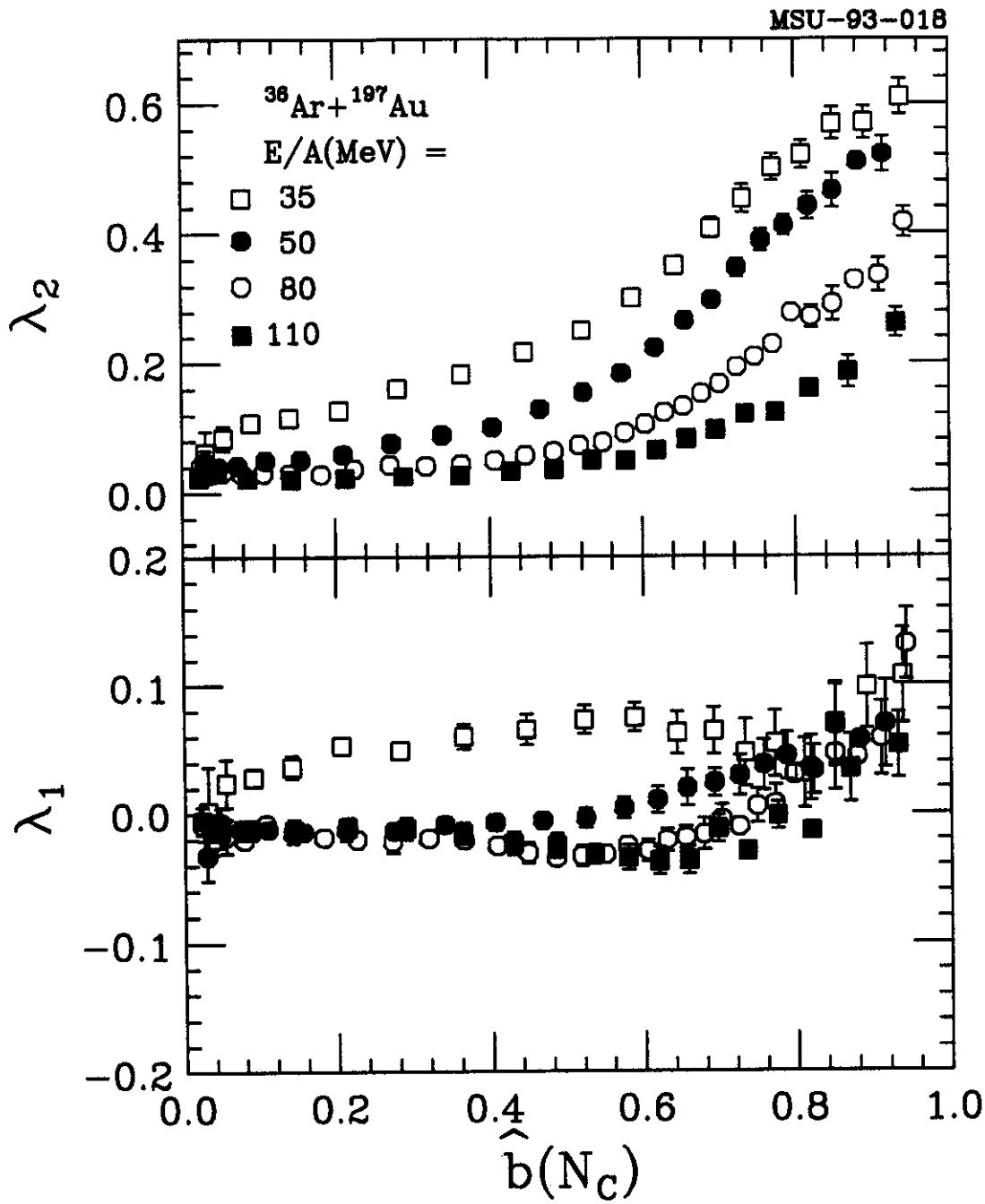
MSU-93-018
$^{36}Ar+^{197}Au$
E/A(MeV) =
35
50
80
110
λ_2
λ_1
$\hat{b}(N_c)$
0.6
0.4
0.2
0.0
0.2
0.1
0.0
−0.1
−0.2
0.0
0.2
0.4
0.6
0.8
1.0

Fig. 7

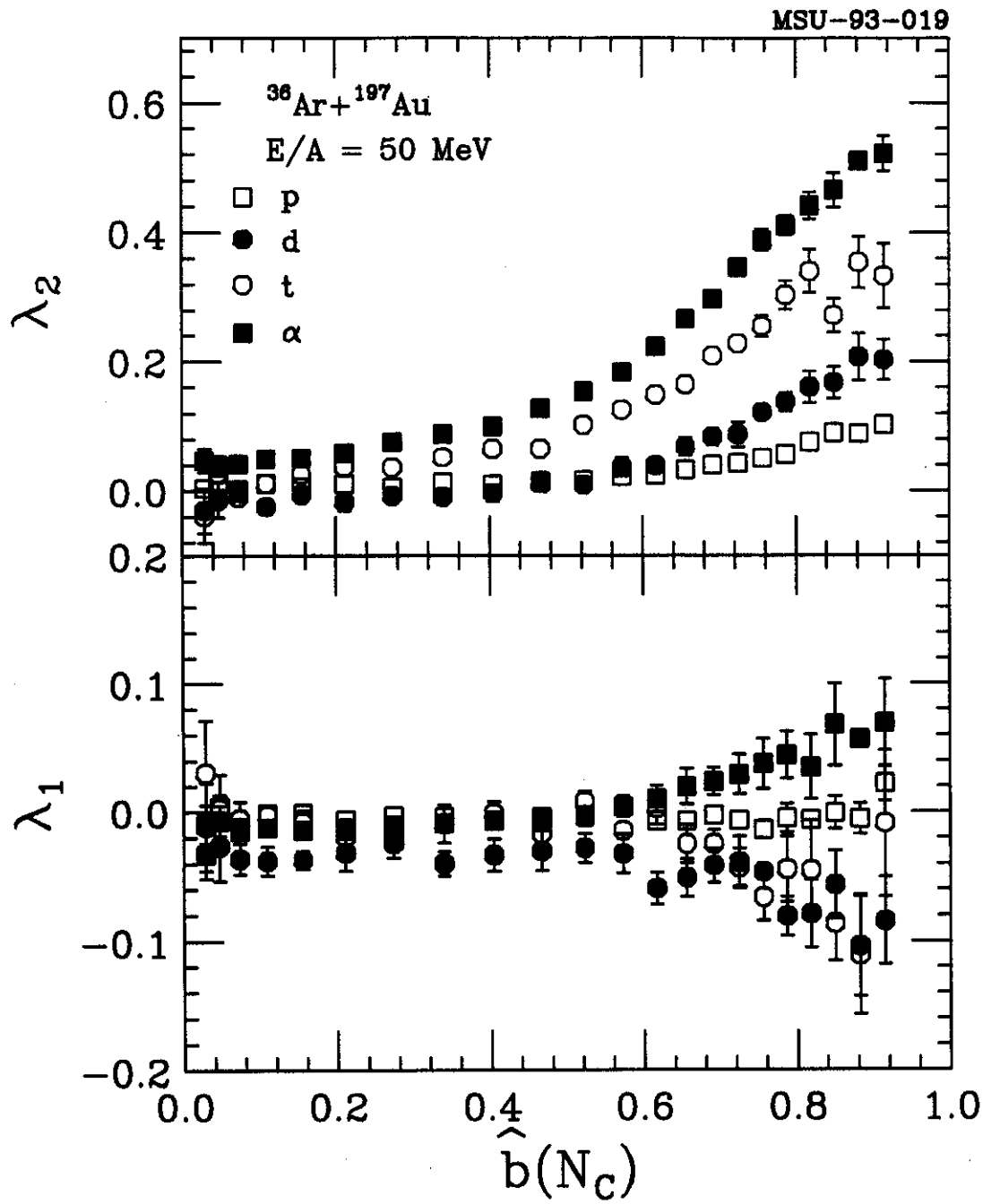
MSU-93-019
^{36}Ar+^{197}Au
E/A = 50 MeV
p
d
t
α
λ_2
λ_1
$\hat{b}(N_c)$
0.6
0.4
0.2
0.0
0.2
0.1
0.0
−0.1
−0.2
0.0
0.2
0.4
0.6
0.8
1.0

Fig. 8

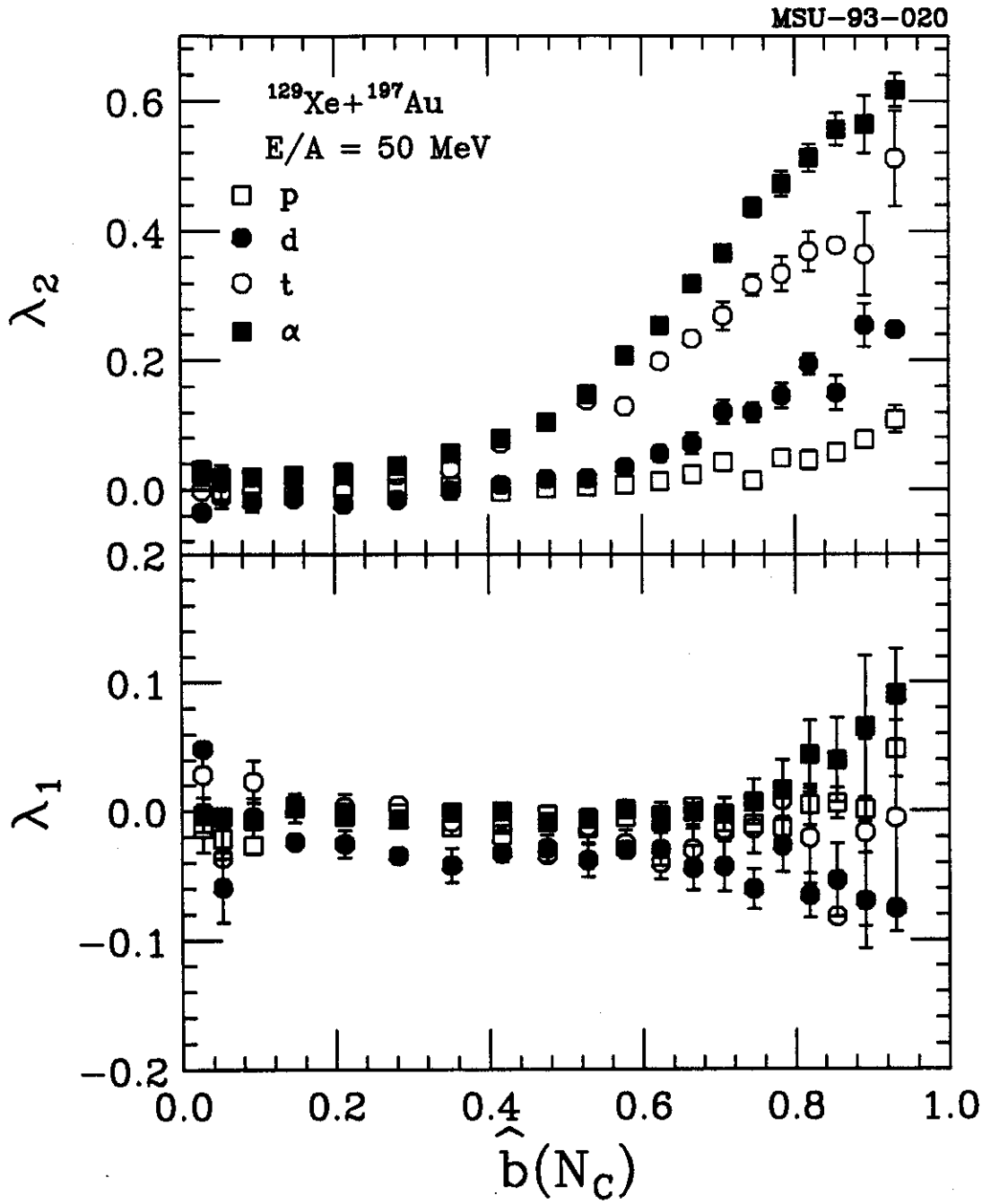
MSU-93-020
^{129}Xe+^{197}Au
E/A = 50 MeV
p
d
t
α
λ_2
λ_1
$\hat{b}(N_c)$
0.6
0.4
0.2
0.0
0.2
0.1
0.0
−0.1
−0.2
0.0
0.2
0.4
0.6
0.8
1.0

Fig. 9

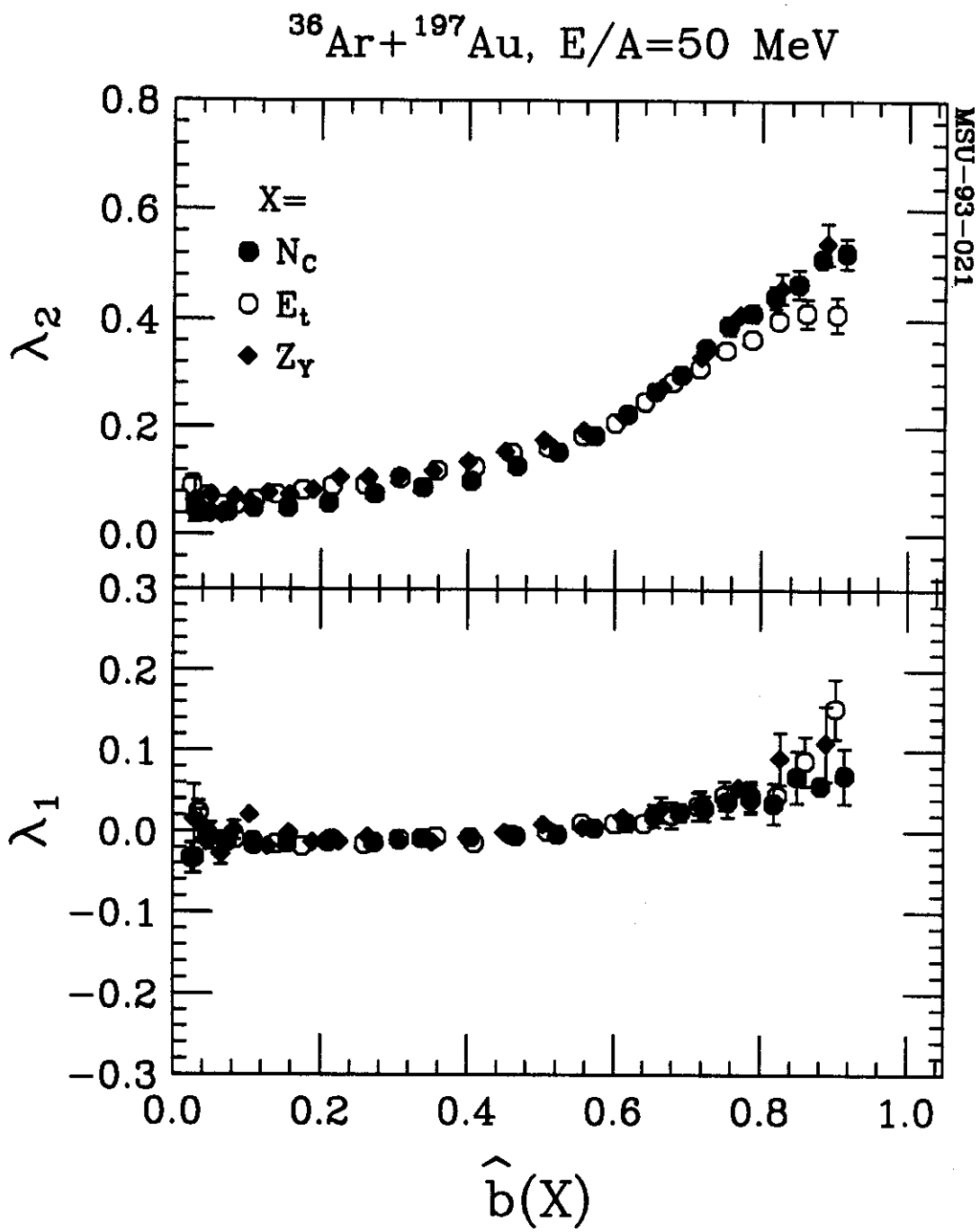
^{36}Ar+^{197}Au, E/A=50 MeV
MSU-93-021
X=
N_C
E_t
Z_Y
λ_2
λ_1
$\hat{b}(X)$
0.8
0.6
0.4
0.2
0.0
0.3
0.2
0.1
0.0
−0.1
−0.2
−0.3
0.0
0.2
0.4
0.6
0.8
1.0

Fig. 10

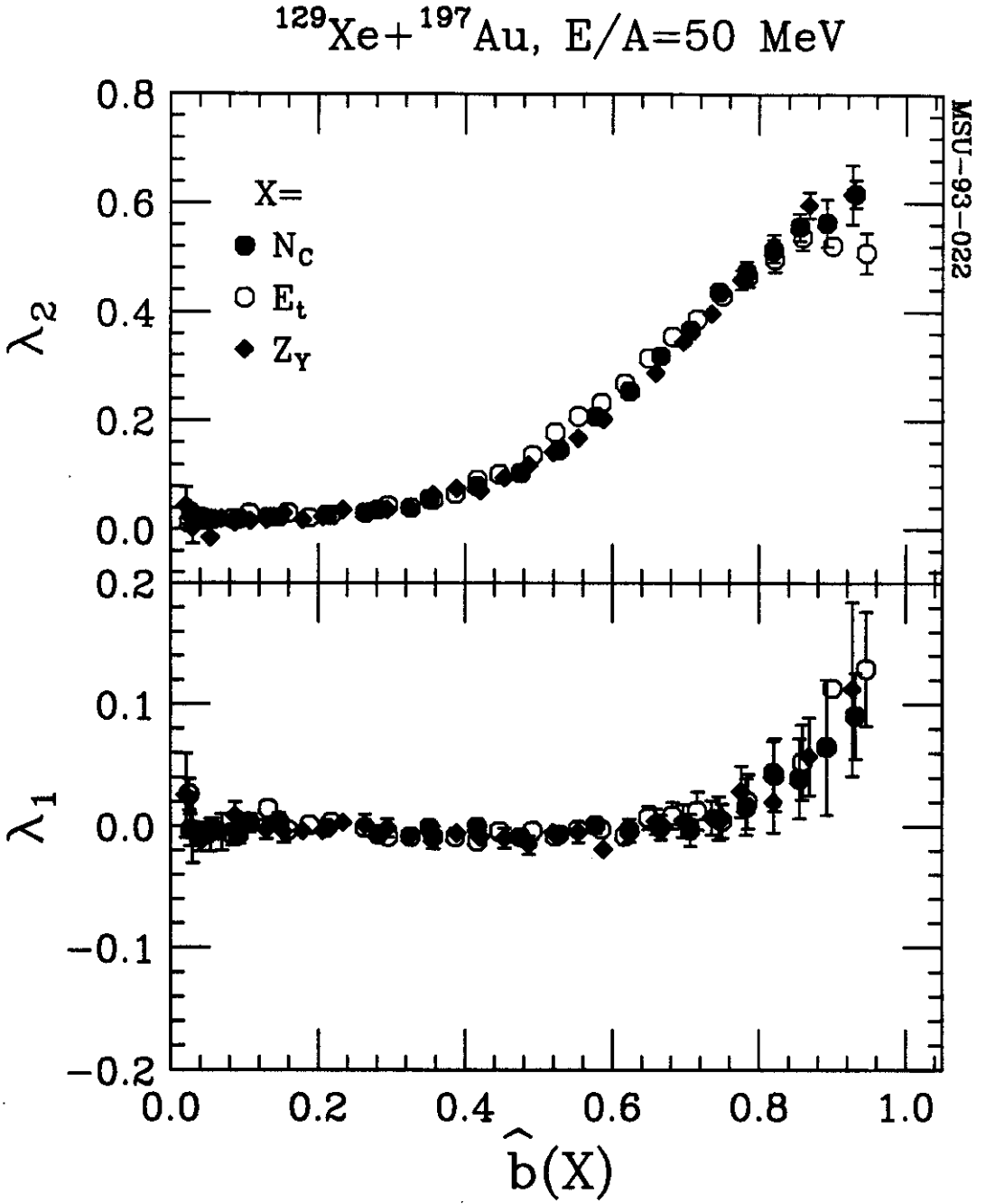
^{129}Xe+^{197}Au, E/A=50 MeV
MSU-93-022
X=
N_C
E_t
Z_Y
λ_2
λ_1
$\hat{b}(X)$
0.8
0.6
0.4
0.2
0.0
0.2
0.1
0.0
−0.1
−0.2
0.0
0.2
0.4
0.6
0.8
1.0

Fig. 11

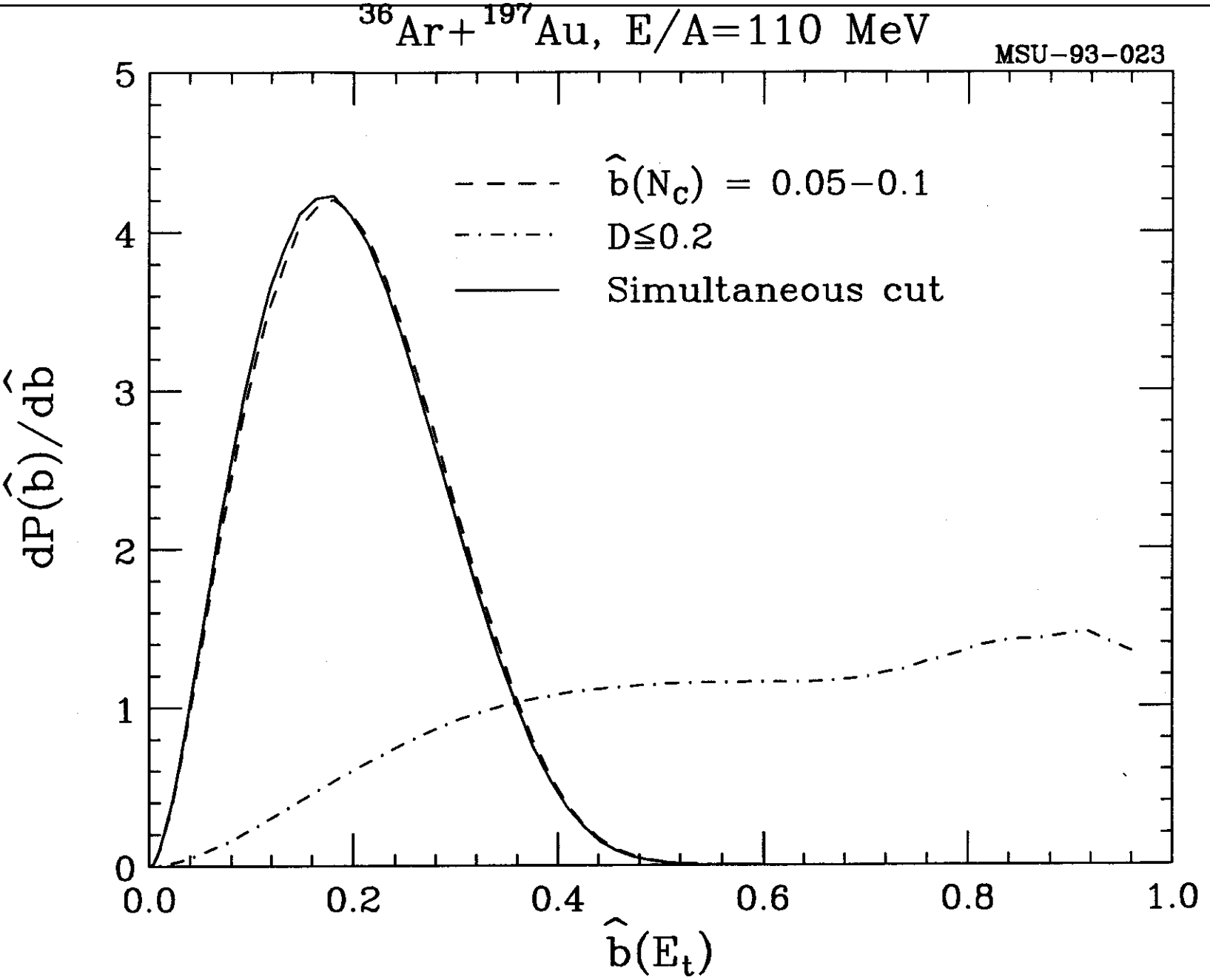
$^{36}Ar+^{197}Au$, E/A=110 MeV
MSU-93-023
$\hat{b}(N_c)$ = 0.05−0.1
D≦0.2
Simultaneous cut
$dP(\hat{b})/d\hat{b}$
$\hat{b}(E_t)$
0
1
2
3
4
5
0.0
0.2
0.4
0.6
0.8
1.0

Fig. 12

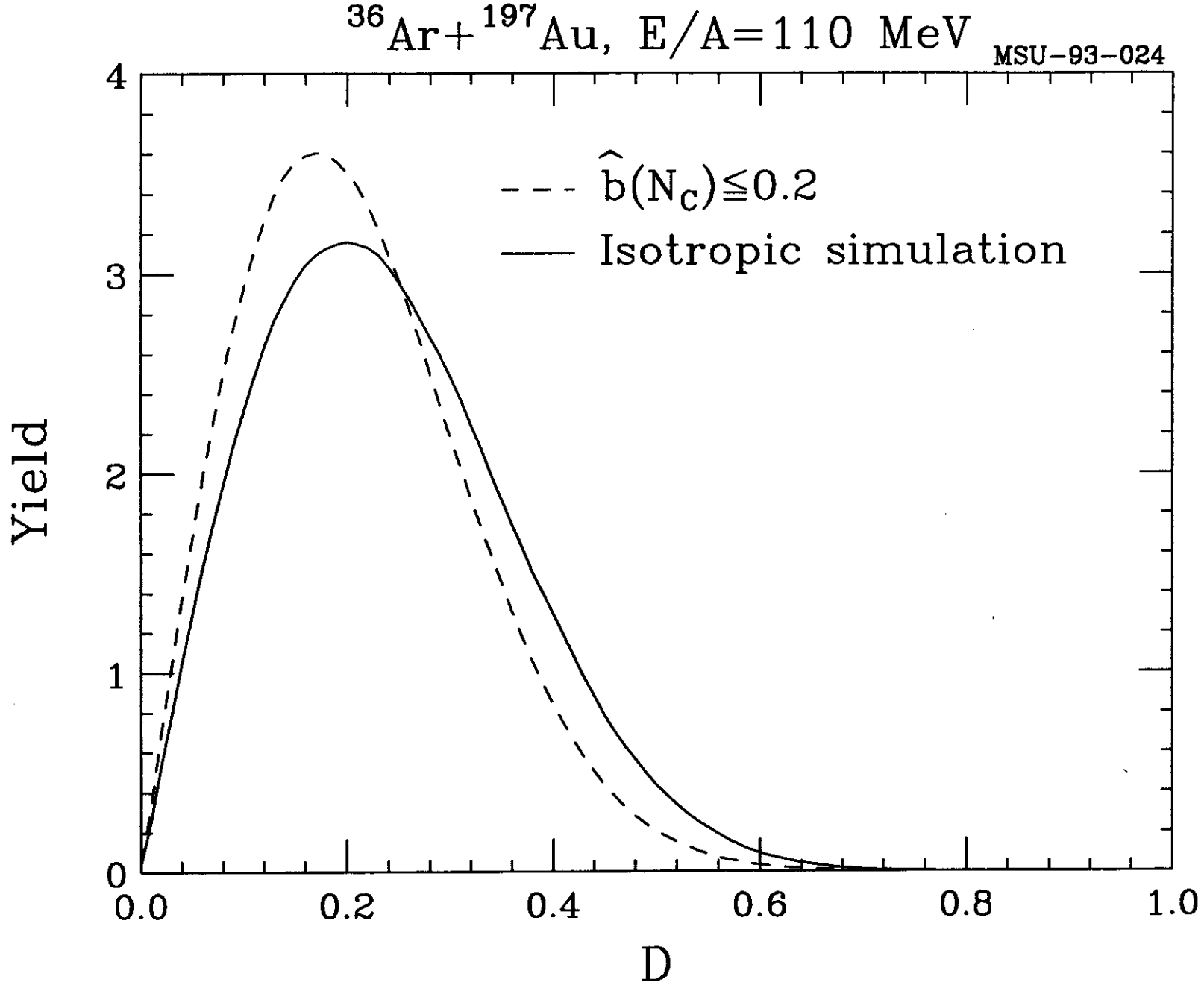
$^{36}Ar+^{197}Au$, E/A=110 MeV
MSU-93-024
$\hat{b}(N_c)\leqq 0.2$
Isotropic simulation
Yield
D
0
1
2
3
4
0.0
0.2
0.4
0.6
0.8
1.0

Fig. 13